Asian Journal of Chemistry; Vol. 38, No. 10 (2026), 2779-2788
ASIAN JOURNAL OF CHEMISTRY
https://doi.org/10.14233/ajchem.2026.36688

Structural, Optical and Magnetic Properties of Samarium Doped Cobalt Ferrite Nanoparticles for Photocatalytic Applications

SWAPNIL A. BHAGAT[1,*], KAJAL A. GURAV[1], SUBHASH M. WANI[2], PRATIK S. PATIL[3], VITTHAL VINAYAK[4], A.P. KECHE[5] and K.M. JADHAV[3,6]

[1]Department of Physics, Deogiri College, Chhatrapati Sambhajinagar-431001, India
[2]Department of Physics, R.G. Bagdia Arts, S.B. Lakhotia Commerce and R. Bezonji Science College, Jalna-431203, India
[3]Department of Physics, Dr. Babasaheb Ambedkar Marathwada University, Chhatrapati Sambhajinagar-431004, India
[4]Department of Industrial Chemistry, Shri. Chhatrapati Shivaji College, Omerga-413606, India
[5]Department of Physics, R.B. Attal Arts, Science and Commerce, Georai, Beed-431127, India
[6]Department of Physics, School of Basic and Applied Sciences, MGM University, Chhatrapati Sambhajinagar-431001, India

*Corresponding author: E-mail: swapniilbhagat@gmail.com

Received: 23 June 2026 *Accepted*: 1 October 2026 *Published online*: 9 October 2026 AJC-22510

In the present work, Sm^{3+} doped spinel cobalt ferrite ($CoFe_2O_4$) nanoparticles [$CoFe_{2-x}Sm_xO_4$ (x = 0.00 to 0.10, with an increment of 0.02)] were fabricated using glycine assisted sol-gel self-ignition method, to understand the effect of Sm^{3+}. The single phase, cubic spinel ferrite phase of the prepared NPs was characterized with the X-ray diffraction (XRD). FTIR spectra confirm the appearance of absorption bands at 554-550 cm^{-1} and 401-389 cm^{-1}. FE-SEM and HR-TEM observations revealed nearly uniform nanoparticles with slight changes in particle morphology upon Sm^{3+} incorporation. Elemental diffraction spectra (EDS) show the elements of cobalt (Co), ferric (Fe), samarium (Sm) and oxygen (O) ions with varying intensity. BET analysis demonstrated variation in the specific surface area associated with particle growth. Optical measurements showed a gradual decrease in band gap energy with increasing Sm^{3+} incorporation. Magnetic measurements confirmed the ferrimagnetic behavior of all samples. The saturation magnetization (M_s) decreased from 77.32 to 60.17 emu g^{-1}, while the coercivity (H_c) increased from 1279.0 to 1752.7 Oe. These changes indicate that Sm^{3+} substitution influences the magnetic response of $CoFe_{2-x}Sm_xO_4$ nanoparticles. Sm^{3+} doping at x = 0.10 improved the photocatalytic efficiency from 86.6% to 88.2%. The changes in structural, optical and magnetic characteristics with Sm^{3+} substitution were accompanied by improved photocatalytic performance, which support the suitability of $CoFe_{2-x}Sm_xO_4$ nanoparticles for photocatalytic applications.

Keywords: Cobalt ferrite, Samarium, Doping, Sol-gel, Photocatalysis.

INTRODUCTION

Spinel ferrites are ferrimagnetic materials that combine electrical insulating and magnetic conducting characteristics [1-3]. Their general chemical formula is MFe_2O_4, where M represents a divalent metal ion [4-6]. At the nanoscale, ferrites possess a high surface-area-to-volume ratio, which strongly influences their electrical and magnetic characteristics [7,8]. Spinel ferrite nanoparticles have been investigated for magnetic recording [9], microwave devices [10], sensors [11], catalysis [12], wastewater treatment [13], biomedical applications [14], energy storage [15,16] and photocatalysis [17]. Their chemical stability, low toxicity, corrosion resistance and relatively simple synthesis further support their use in scientific and technological applications [18].

Among spinel ferrites, cobalt ferrite ($CoFe_2O_4$) is one of the most extensively studied materials owing to its ferrimagnetic, electrical, dielectric, optical mechanical and catalytic properties [19,20]. It possesses high electrical resistivity, low eddy-current and dielectric losses, tunable magnetic characteristics, good chemical stability and high mechanical hardness [21], which are associated with its inverse-spinel structure [22]. The magnetic interactions between the tetrahedral (A) and octahedral [B] sites play an important role in determining its magnetic behaviour. $CoFe_2O_4$ further exhibits good thermal stability and electrical resistivity, making it

This is an open access journal, and articles are distributed under the terms of the Attribution 4.0 International (CC BY 4.0) License. This license lets others distribute, remix, tweak, and build upon your work, even commercially, as long as they credit the author for the original creation. You must give appropriate credit, provide a link to the license, and indicate if changes were made.

useful in permanent magnets, magnetic sensors, electromagnetic interference shielding, biomedical applications, photocatalysis, and other multifunctional systems [23-25]. Its physico-chemical properties can be modified through cation substitution. The incorporation of suitable metal ions alters cation distribution among the available lattice sites and can modify the lattice parameter, crystallite size, crystallinity, magnetic exchange interactions, optical band gap and electrical conductivity [26].

Rare-earth ions have attracted considerable interest as dopants for spinel ferrites owing to their relatively large ionic radii, partially filled 4*f*-orbitals and strong spin-orbit coupling [27]. Their incorporation can introduce lattice distortion, influence grain growth, modify magnetic anisotropy and alter optical properties [28], making rare-earth-substituted ferrites relevant to magnetic, electronic, optical, and energy-related applications [29,30]. Among these dopants, samarium (Sm^{3+}) is particularly interesting for $CoFe_2O_4$. Its larger ionic radius can introduce lattice strain and structural distortion when incorporated into the ferrite lattice [31]. Such changes may affect crystallite growth, cation distribution and magnetic interactions. The partially filled 4*f*-orbital of Sm^{3+} can contribute to magnetic anisotropy and modify coercivity and saturation magnetization [32]. Sm^{3+} substitution may further influence optical absorption through the formation of localized energy states, leading to changes in the optical band gap.

Several studies have reported the synthesis of Sm^{3+}-doped $CoFe_2O_4$ nanoparticles using different chemical routes, with changes in structural, magnetic and optical properties [33-35]. The incorporation of Sm^{3+} has generally been associated with an increase in lattice parameters owing to its larger ionic size, while its effect on crystallite size depends on the synthesis conditions and dopant concentration [36,37]. The variations in saturation magnetization and coercivity have been linked to changes in cation distribution and magnetic exchange interactions [38]. Optical studies have reported changes in the band gap with Sm^{3+} incorporation [39]. Despite these reports, comprehensive studies systematically correlating structural, morphological, optical, surface and magnetic characteristics over a well-defined Sm^{3+} concentration range remain relatively limited [40,41]. Since the preparation conditions can affect the resulting structural, optical and magnetic properties, systematic studies under identical synthesis conditions are needed to clarify the role of Sm^{3+} substitution [42].

The sol-gel auto-combustion method is a simple and cost-effective route for synthesizing ferrite nanoparticles [43-45]. It provides good chemical homogeneity, compositional control, short processing time and fine, highly pure nanoparticles at relatively low temperatures [46-48]. Molecular-level mixing of metal precursors promotes uniform cation distribution, while self-propagating combustion facilitates rapid crystallization, making the method suitable for rare-earth-substituted spinel ferrites [49].

The present study focuses on establishing a systematic relationship between Sm^{3+} concentration and the structural, morphological, optical, surface, magnetic and photocatalytic properties of $CoFe_2O_4$ nanoparticles prepared by a sol-gel auto-combustion method. Sm^{3+}-doped cobalt ferrite nanoparticles with the composition $CoFe_{2-x}Sm_xO_4$ (x = 0.00-0.10, with increments of 0.02) were synthesized by the sol-gel auto-combustion method. The effect of Sm^{3+} substitution on the physicochemical properties of the nanoparticles was investigated, with particular emphasis on their photocatalytic performance for dye degradation.

EXPERIMENTAL

All reagents were used as received without further purification. $CoFe_{2-x}Sm_xO_4$ (x = 0.00-0.10, in increments of 0.02) nanoparticles were prepared using cobalt, samarium and ferric nitrates with 99% purity. Glycine served as the chelating agent, while aqueous ammonia was used to adjust the pH. Each metal nitrate was separately dissolved in 200 mL of distilled water.

Synthesis of Sm^{3+} doped $CoFe_2O_4$: Sm^{3+}doped cobalt ferrite nanoparticles ($CoFe_{2-x}Sm_xO_4$; x = 0.00 to 0.10, in the steps of 0.02) were prepared by the sol-gel self-ignition method using glycine as the fuel. The metal nitrates were separately dissolved in distilled water, followed by the addition of glycine as a chelating agent. The metal nitrate-to-glycine (fuel) ratio was maintained at 1:4.4. The pH was adjusted to 7 by adding NH_3 solution dropwise, and the mixture was stirred until a homogeneous sol formed. The sol was heated at 75-85 ºC until a thick gel formed. Further heating caused the gel to self-ignite and yield a loose powder. The powder was then ground and sintered at 600 ºC for 3 h to remove residual organic matter and develop the crystalline spinel ferrite phase.

Photocatalytic degradation of dye: The prepared typical Sm^{3+} doped $CoFe_2O_4$ nanoparticles were explored to photocatalytic rhodamine B (Rh-B) dye degradation. The nanoparticles were dispersed in Rh-B solution and mixed thoroughly using magnetic stirrer. The solution was then kept in a dark for enrich absorption and desorption process. A 50 mL solution was exposed to direct sunlight in an open environment during the period of maximum sunlight intensity. UV–Vis absorption measurements were recorded at regular time intervals to monitor the photocatalytic degradation. The experiments were carried out during the summer season at MGM University, Chhatrapati Sambhajinagar.

Characterization: The structural, morphological, surface, optical, magnetic and antibacterial properties of $CoFe_{2-x}Sm_xO_4$ (x = 0.00-0.10, in increments of 0.02) nanoparticles were investigated using standard analytical techniques. XRD patterns were recorded at 300 K over 2θ = 20-80º using Cu*K*α radiation (λ = 1.5406 Å) on a Bruker D8 Advance diffractometer. FTIR spectra were obtained at 300 K in the range of 4000-400 cm^{-1} using a PerkinElmer spectrophotometer. FE-SEM (JEOL JSM-7600F) and HR-TEM (JEOL JEM-2100 Plus) were used to examine morphology and particle size. BET surface area and pore characteristics were measured using a Micromeritics ASAP 2020 analyzer. UV–Vis spectra were recorded from 200-900 nm using a Perkin-Elmer Lambda 950 spectrophotometer and the optical band gap was estimated from Tauc plots. Magnetic properties were evaluated from M–H hysteresis curves at 300 K using a Microsense EZ9 VSM.

RESULTS AND DISCUSSION

X-ray diffraction (XRD): Fig. 1 presents the XRD patterns of $CoFe_{2-x}Sm_xO_4$ (x = 0.00, 0.02, 0.04, 0.06, 0.08 and 0.10), which are consistent with the standard pattern of $CoFe_2O_4$ (ICDD file No. 22-1086) [50]. The reflections at 2θ values corresponding to the (220), (311), (222), (400), (422), (511) and (440) planes are characteristic of the cubic spinel structure of cobalt ferrite. No additional reflections associated with secondary phases were detected throughout the studied Sm^{3+} concentration range. The sharp and well-defined peaks indicate good crystallinity and the formation of a single spinel phase.

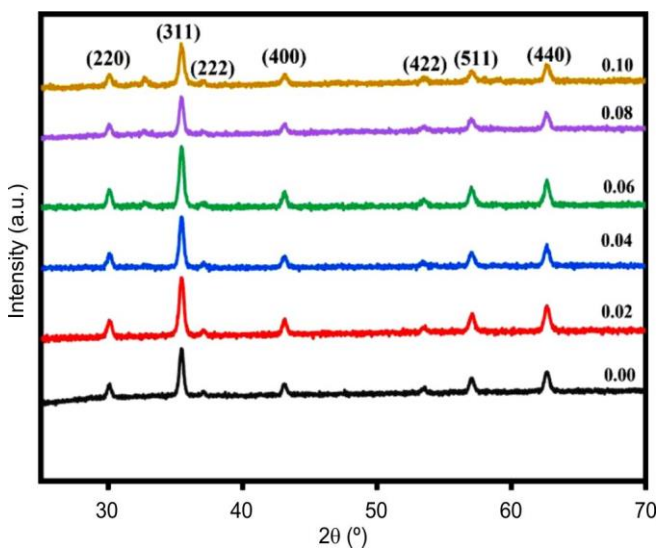

Fig. 1. X-ray diffraction pattern for $CoFe_{2-x}Sm_xO_4$ (x = 0.00, 0.02, 0.04, 0.06, 0.08, 0.10) NPs

A slight shift of the diffraction peaks toward lower 2θ values is observed with increasing Sm^{3+} content, as listed in Table-1. This shift can be related to the incorporation of the larger Sm^{3+} ions into the $CoFe_2O_4$ lattice, which causes a small expansion of the crystal lattice. For the cubic spinel structure, the lattice parameter can be calculated using the following equation [51].

In a cubic structure, the lattice constants are identical in size and can be described by the below equation [51]:

$$a = d_{hkl}\sqrt{N} \quad (1)$$

where notations have their usual meaning.

$$N = (h^2 + k^2 + l^2) \quad (2)$$

The obtained values of lattice constant (a) are given in Table-1. The 'a' for pure cobalt ferrite (8.379 Å) aligns well with the values found in existing literature [52,53]. The lattice constant shows a small but clear change with Sm^{3+} doping from 8.379 Å (x = 0.0) and then it increases gradually to a maximum of 8.389 Å (x = 0.10). The lattice parameter increases gradually up to x = 0.08, which can be attributed to the incorporation of the larger Sm^{3+} ions into the $CoFe_2O_4$ lattice. Their larger ionic size may increase the separation between neighbouring ions and expand the unit cell. A slight decrease in the lattice parameter at x = 0.10 may arise from increased lattice strain or defect accommodation at higher Sm^{3+} content. The variation of the lattice parameter (a) with Sm^{3+} concentration (x) is shown in Fig. 2.

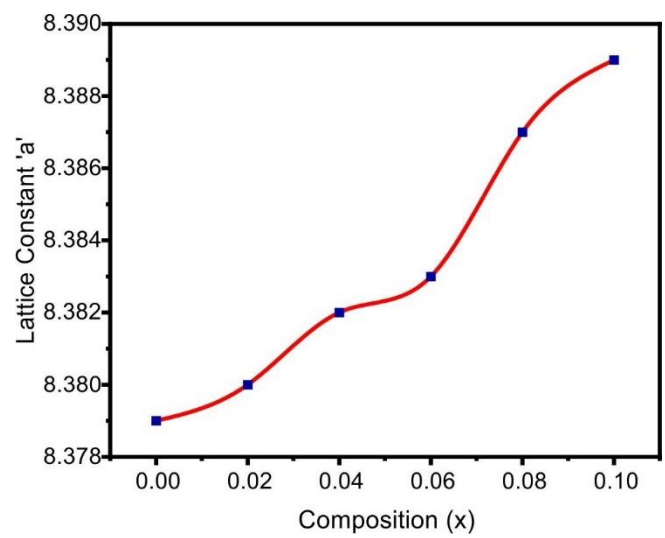

Fig. 2. Variation of lattice constant (a) with composition (x) of $CoFe_{2-x}Sm_xO_4$ (x = 0.00, 0.02, 0.04, 0.06, 0.08, 0.10) of NPs

The crystallite size (t) was estimated from the broadening of the (311) reflection using the Scherrer equation [54]:

$$t = \frac{K\lambda}{\beta\cos\theta} \quad (3)$$

The crystallite sizes remain almost same (22-23 nm) for all the Sm^{3+} doped cobalt ferrite nanoparticles. The dislocation density (δ) and microstrain (ε) show small changes across the compositions, following the trend observed for crystallite size (Table-1). Samples with smaller crystallite sizes generally exhibit slightly higher dislocation density and microstrain. The values of δ and ε were calculated using the following relations [51]:

TABLE-1
VALUES OF LATTICE CONSTANT (a), CRYSTALLITE SIZE (t), X-RAY DENSITY (d_x), DISLOCATION DENSITY (δ), MICRO STRAIN (ε) FOR $CoSm_xFe_{2-x}O_4$ (x = 0.00, 0.02, 0.04, 0.06, 0.08, 0.10) NPs

x	2θ (311) plane	a (Å)	t (nm)	d_x (g/cc)	δ × 10^{-3} (lines/m^2)	ε × 10^{-3}
0.00	35.48	8.379	23	5.297	1.8963	4.0586
0.02	35.46	8.380	20	5.339	2.4636	4.7098
0.04	35.45	8.382	22	5.377	1.7409	3.7960
0.06	35.45	8.383	20	5.418	2.0643	4.1969
0.08	35.44	8.387	22	5.453	2.2332	4.4618
0.10	35.43	8.389	20	5.509	2.2709	4.4821

$$\delta = \frac{1}{t^2} \quad (4)$$

$$\varepsilon = \frac{\beta}{4\tan\theta} \quad (5)$$

The X-ray density (d_x) increases from 5.297 g cm^{-3} for x = 0.00 to 5.509 g cm^{-3} for x = 0.10 (Table-1). This increase can be attributed to the higher atomic mass of Sm^{3+} relative to Fe^{3+}, which raises the mass of the unit cell despite the small changes in lattice parameter.

FTIR: Fig. 3 shows the FTIR spectra of $CoFe_{2-x}Sm_xO_4$ (x = 0.00-0.10) nanoparticles, with characteristic absorption bands observed in the ranges of 555-550 cm^{-1} (ν_1) and 402-389 cm^{-1} (ν_2) [55]. These bands are assigned to the metal–oxygen (M–O) stretching vibrations at the tetrahedral (A) and octahedral [B] sites, respectively [56]. The slight shifts in ν_1 and ν_2 with increasing Sm^{3+} content indicate changes in the local lattice environment caused by the substitution of the larger Sm^{3+} ions for Fe^{3+} ions. The non-linear variation in band positions may arise from small changes in Fe–O and Co–O bond lengths and redistribution of cations between the (A) and [B] sites [55]. The observed band broadening is associated with the nanocrystalline nature of the samples and lattice strain arising from crystallite size reduction and Sm^{3+} incorporation. The absorption band values are listed in Table-2 and are consistent with previous reports on Sm^{3+}-doped cobalt ferrite nanoparticles.

FE-SEM: The surface morphology, grain size distribution and EDS elemental mapping of Sm^{3+}-doped $CoFe_2O_4$ NPs are shown in Fig. 4a-c, respectively. FE-SEM images analysis shows agglomeration with spherical grains. The observed agglomeration can be attributed to magnetic interactions between Fe^{2+} and Fe^{3+} ions, along with the high surface energy of the fine particles. The particles exhibit a relatively porous and uniform morphology, which may be favourable for catalytic and magnetic applications by providing a larger accessible surface area. The grain-size distribution histograms place the particles within the nanometer range, with average grain sizes of 36.44, 35.55 and 36.20 nm and a relatively narrow distribution. A gradual decrease in grain size is observed with increasing Sm^{3+} concentration, which suggest that Sm^{3+} substitution limits grain growth during crystallization. The larger Sm^{3+} ions replacing Fe^{3+} introduce local lattice distortion and strain, which can restrict the growth of crystallites. The EDS spectra show the characteristic signals of Co, Fe, O and Sm, with no additional peaks attributable to detectable impurities. The morphological results show a slight reduction in grain size with Sm^{3+} incorporation, while the spinel ferrite retains its structural integrity and uniform elemental composition.

HR-TEM: The HR-TEM image for the typical composition x = 0.06 and particle size histogram (Fig. 5a-b) confirm that the synthesized nanoparticles are indeed in the nanoscale

TABLE-2
VALUES OF ABSORPTION BANDS (ν_1 AND ν_2) FOR FTIR SPECTRUM OF $CoSm_xFe_{2-x}O_4$ (x = 0.00, 0.02, 0.04, 0.06, 0.08, 0.10) NPs

x	ν_1 (cm^{-1})	ν_2 (cm^{-1})
0.00	550	401
0.02	555	402
0.04	553	389
0.06	547	389
0.08	549	392
0.10	554	389

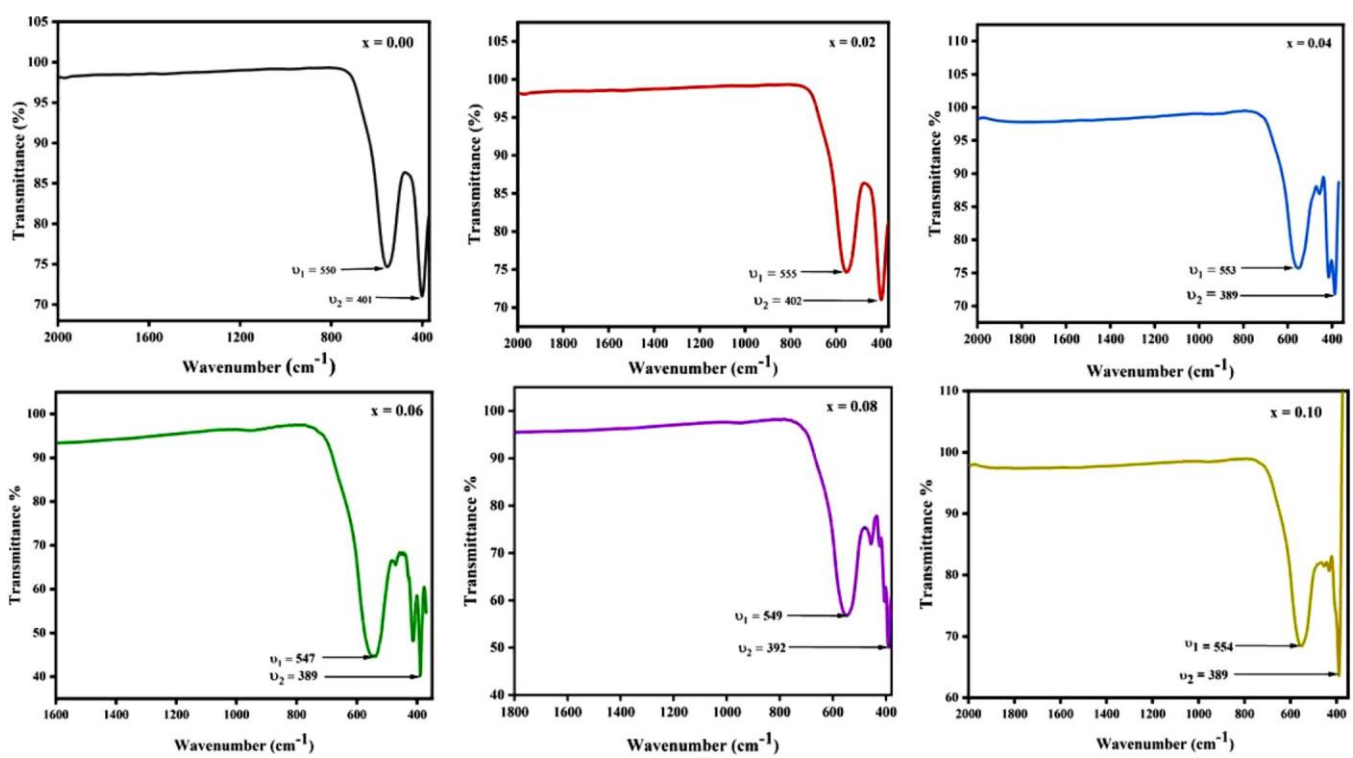

Fig. 3. FTIR spectra of $CoSm_xFe_{2-x}O_4$ (x = 0.00, 0.02, 0.04, 0.06, 0.08, 0.10) NPs

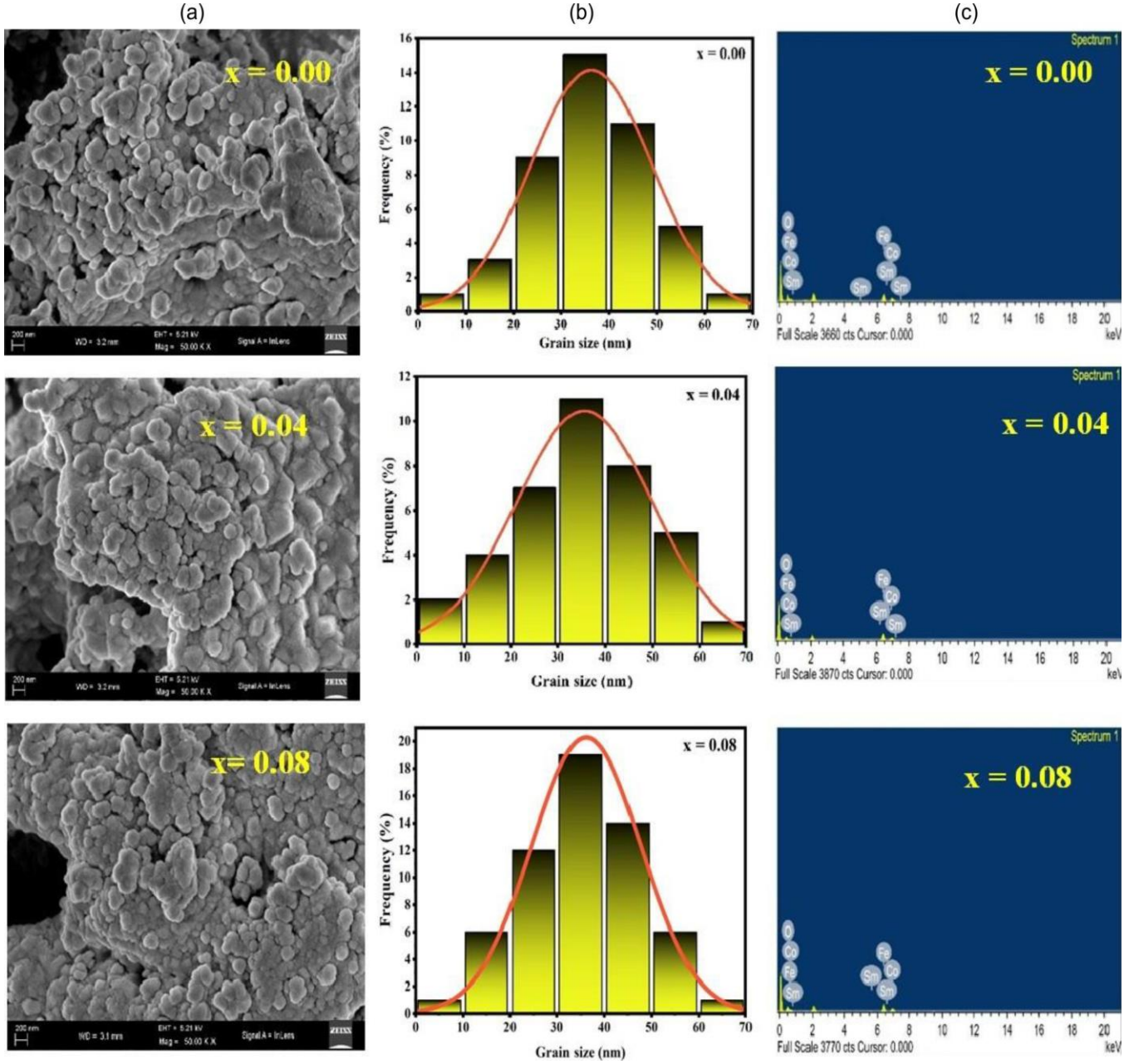

Fig. 4. (a) FE-SEM images, (b) histogram (c) EDX spectra of $CoSm_xFe_{2-x}O_4$ (x = 0.00, 0.04, 0.08) NP

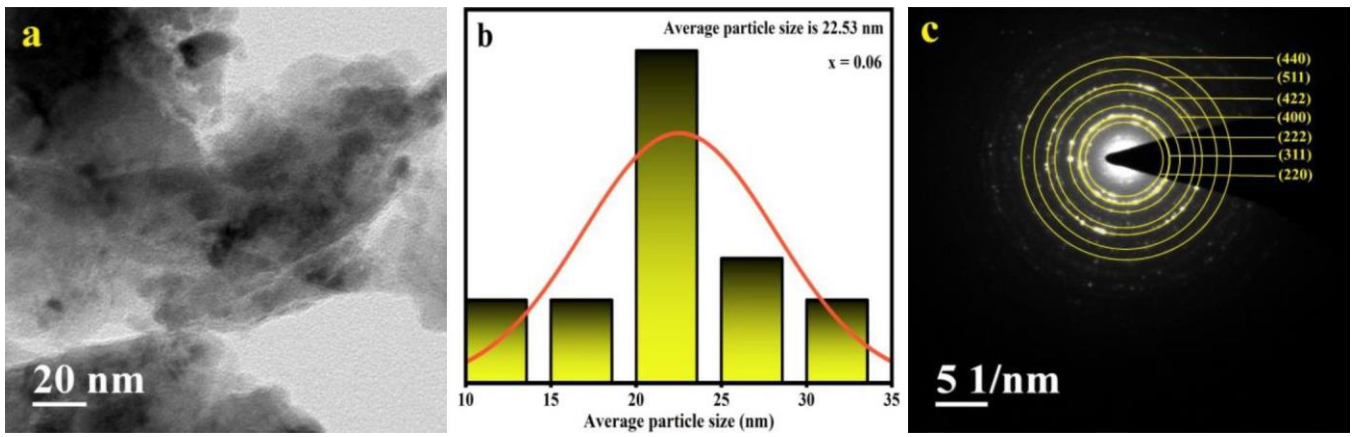

Fig. 5. (a) HR-TEM image, (b) histogram of average particle size and (c) SAED pattern of $CoSm_xFe_{2-x}O_4$ (x = 0.06) NPs

range, with particle size of 22.53 nm. The particle-size distribution histogram is relatively narrow, which points to fairly uniform nucleation and particle growth during synthesis. The TEM micrograph contains small particles with nearly spherical to irregular shapes together with some partially agglomerated regions. Such clustering is expected for magnetic oxide nanoparticles, where magnetic attraction and high surface energy promote particle-particle interactions. Individual particles and small clusters can still be distinguished and their appearance is consistent with the particle-size distribution obtained from the histogram.

The selected-area electron diffraction (SAED) pattern in Fig. 5c consists of distinct concentric rings with bright spots, characteristic of a polycrystalline material containing numerous small crystallites. The rings can be indexed to the characteristic (*hkl*) planes of the spinel ferrite structure, confirming the crystalline nature of the synthesized particles. The lattice fringes visible in the HR-TEM image provide further evidence of crystallinity at the local level. The TEM, SAED and HR-TEM observations together confirm the formation of nanocrystalline spinel ferrite particles with a relatively uniform particle size and well-preserved crystal structure.

BET measurements: BET measurements based on N_2 adsorption–desorption isotherms at 77 K were carried out to examine the textural properties of Sm^{3+}-doped $CoFe_2O_4$ nanoparticles at different dopant concentrations (x = 0.00, 0.04 and 0.08). The corresponding isotherms are shown in Fig. 6, while the specific surface area, average pore diameter and total pore volume are listed in Table-3. All samples exhibit type IV isotherms with distinct H3-type hysteresis loops, which are generally associated with mesoporous materials containing slit-shaped pores. The pore characteristics obtained from these measurements point to a mesoporous structure in the synthesized ferrite samples, which can provide better surface accessibility for surface-dependent applications such as photocatalysis.

TABLE-3
SURFACE AREA, AVERAGE PORE DIAMETER AND PORE VOLUME OF $CoSm_xFe_{2-x}O_4$ (x = 0.00, 0.04 AND 0.08) NPs

x	Surface area (m^2/g)	Average pore diameter (nm)	Pore volume (cm^3/g)
0.00	11.163	6.775	0.0285
0.04	15.867	5.749	0.0368
0.08	11.205	5.855	0.0259

The undoped $CoFe_2O_4$ sample (x = 0.00) has a BET surface area of 11.163 $m^2\ g^{-1}$. With Sm^{3+} incorporation at x = 0.04, the surface area increases to 15.867 $m^2\ g^{-1}$. This change can be related to the lattice distortion caused by replacing Fe^{3+} with the larger Sm^{3+} ions. Such substitution may introduce local structural disorder and defects, creating additional accessible surface sites. At this moderate dopant level, Sm^{3+} incorporation may further restrict particle growth and improve particle dispersion, which contribute to the higher surface area.

When the Sm^{3+} content is increased to x = 0.08, the surface area falls to 11.205 $m^2\ g^{-1}$, which is close to that of the undoped sample. At higher dopant loading, increased particle agglomeration or partial blockage of the pores may reduce the accessible surface. This behaviour suggests that the effect of Sm^{3+} incorporation on the textural properties is not simply proportional to dopant concentration, with x = 0.04 providing the most favourable surface characteristics among the compositions examined.

A similar trend is observed for the total pore volume. Its value increases from 0.0285 $cm^3\ g^{-1}$ for x = 0.00 to 0.0368 $cm^3\ g^{-1}$ at x = 0.04, before decreasing to 0.0259 $cm^3\ g^{-1}$ at x = 0.08. The maximum pore volume at x = 0.04 supports the higher surface area observed at this composition. The average pore diameter decreases from 6.775 nm for the undoped sample to 5.749 nm at x = 0.04 and then changes slightly to 5.855 nm at x = 0.08. These values remain within the mesoporous range and point to a relatively finer pore structure after Sm^{3+} incorporation. The changes in pore dimensions can be associated with lattice distortion, particle growth behaviour and the development of interparticle pores during synthesis.

Optical properties: The absorption spectra of the synthesized Sm^{3+} doped spinel ferrites are shown in Fig. 7 and were used to determine the absorption coefficient. The optical band gap energy was estimated from the Tauc plots (Fig. 8) using the Tauc relation given in eqn. 6, where the symbols have their usual meanings.

$$(\alpha h\nu)^2 = B(h\nu - E_g) \quad (6)$$

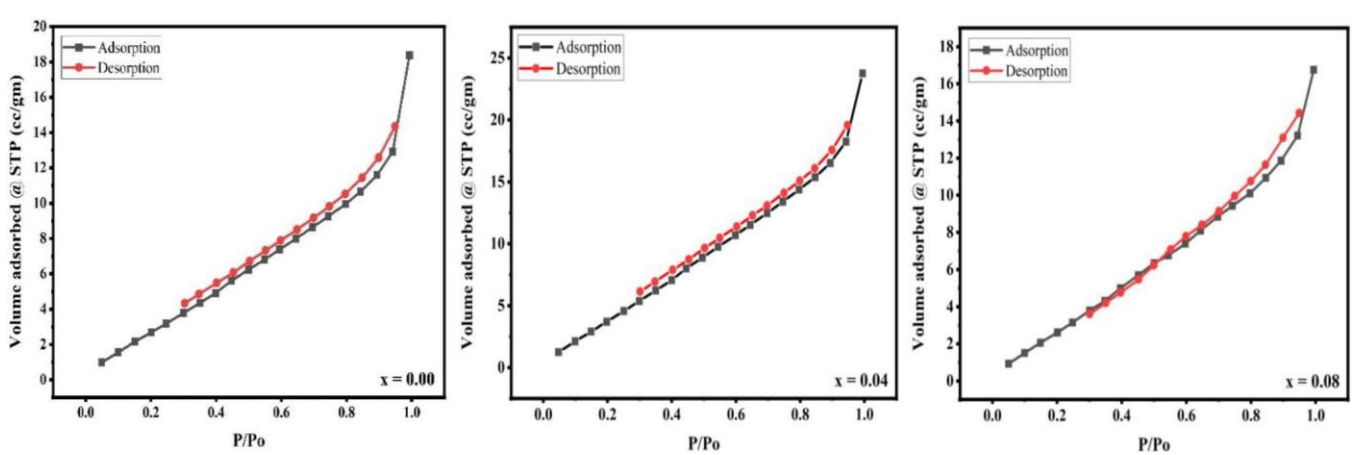

Fig. 6. Adsorption-desorption isotherms of $CoSm_xFe_{2-x}O_4$ (x = 0.00, 0.04 and 0.08) NPs

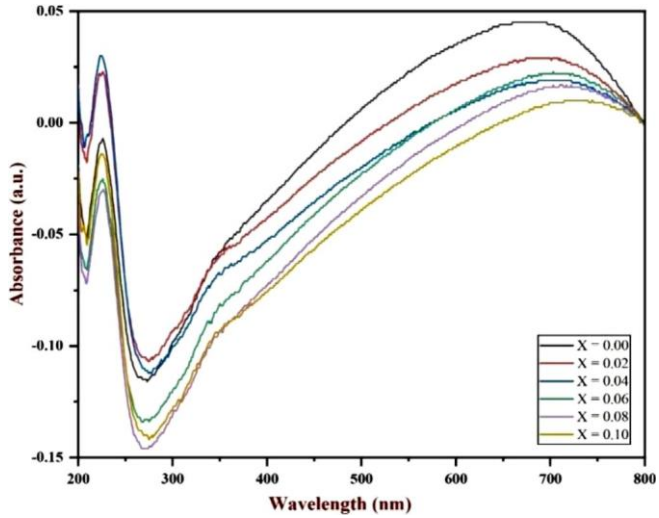

Fig. 7. Absorbance spectra for $CoFe_{2-x}Sm_xO_4$ (x = 0.00, 0.02, 0.04, 0.06, 0.08, 0.10) NPs

The estimated band gap values decrease progressively from 2.69 eV for the undoped $CoFe_2O_4$ sample to 2.63, 2.56, 2.55, 2.50 and 2.23 eV with increasing Sm^{3+} concentration. The band gap obtained for pure $CoFe_2O_4$ is close to previously reported values [31,34] and hence support the reliability of the optical analysis. The gradual reduction in band gap can be related to the substitution of Fe^{3+} ions (0.645 Å) by the larger Sm^{3+} ions (1.079 Å), which disturbs the local crystal environment and modifies the metal–oxygen bonding. This lattice distortion can introduce defect or localized states close to the valence and conduction bands, reducing the energy required for electronic transitions. Similar band-gap narrowing has been reported for rare-earth-doped spinel ferrites, where lattice distortion and dopant-related defect states contribute to stronger absorption in the visible region [5,57].

Magnetic properties: The magnetic properties of $CoFe_{2-x}Sm_xO_4$ (x = 0.00-0.10) nanoparticles were measured at 300 K using a vibrating sample magnetometer (VSM). All compositions exhibit ferrimagnetic behaviour, as observed from the well-defined M–H hysteresis loops in Fig. 9. The corresponding magnetic parameters are listed in Table-4.

TABLE-4
VALUES OF SATURATION MAGNETIZATION (M_s), REMANENCE MAGNETIZATION (M_r), REMANENCE RATIO (M_r/M_s), COERCIVITY (H_c), NET MAGNETIC MOMENT (n_B) OF Sm^{3+} DOPING ON MAGNETIC PARAMETERS OF $CoSm_xFe_{2-x}O_4$ (x = 0.00, 0.02, 0.04, 0.06, 0.08, 0.10) NPs

x	M_s (emu/g)	M_r (emu/g)	R = M_r/M_s	H_c (Oe)	n_B (μB)
0.00	77.32	38.00	0.49	1487.3	3.24
0.02	68.46	31.21	0.45	1279.0	2.89
0.04	74.35	35.29	0.47	1440.1	3.17
0.06	61.88	29.51	0.48	1383.2	2.66
0.08	60.17	30.82	0.51	1752.7	2.60
0.10	70.45	32.65	0.46	1738.7	3.07

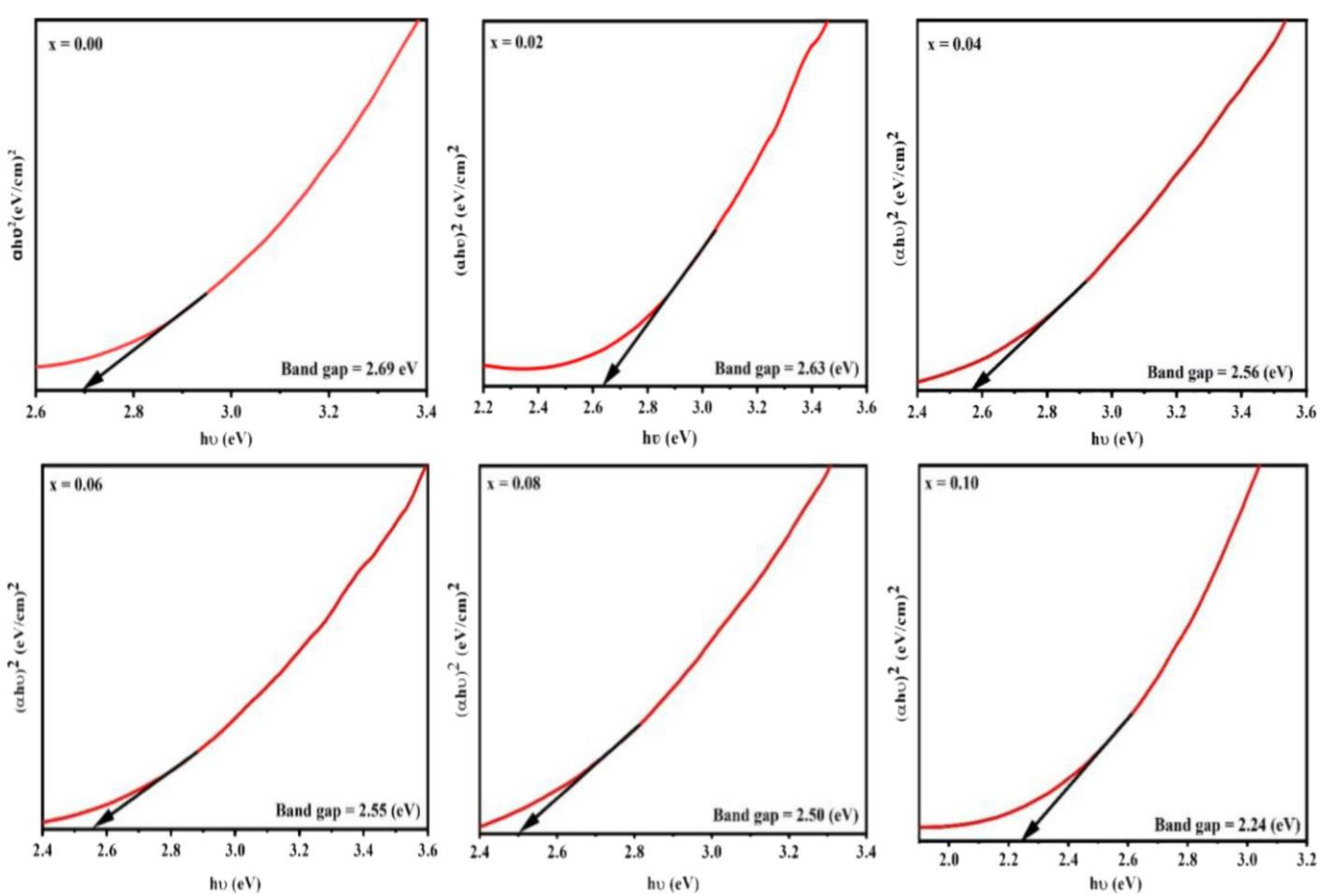

Fig. 8. Tauc plots of $CoSm_xFe_{2-x}O_4$ (x = 0.00, 0.02, 0.04, 0.06, 0.08, 0.10) NPs

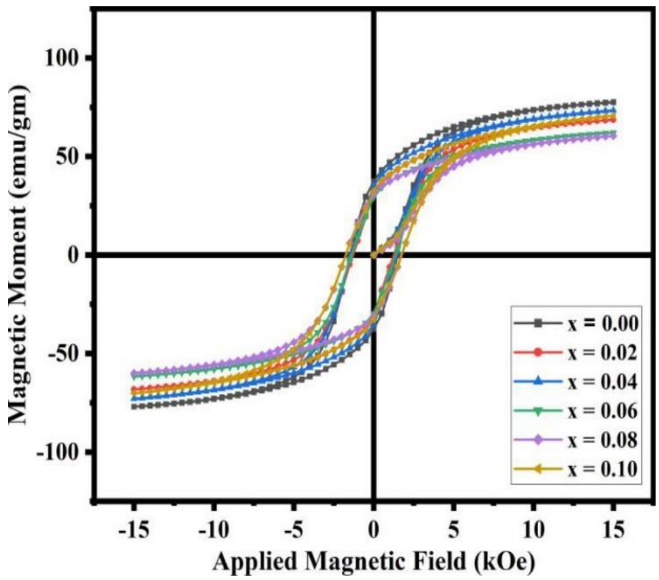

Fig. 9. M-H hysteresis loop of $CoSm_xFe_{2-x}O_4$ (x = 0.00, 0.02, 0.04, 0.06, 0.08, 0.10) NPs

The saturation magnetization (M_s) of the undoped $CoFe_2O_4$ sample (x = 0.00) is 77.32 emu g^{-1}. With Sm^{3+} incorporation, Ms decreases, although the variation is not strictly monotonic across the series. This change can be related to the replacement of magnetic Fe^{3+} ions by Sm^{3+} ions, together with changes in cation distribution between the tetrahedral (A) and octahedral [B] sites. Since, Sm^{3+} contributes little to the net ferrimagnetic moment compared with Fe^{3+}, its incorporation can weaken the A–B super-exchange interaction and alter the balance between the two magnetic sublattices. The irregular variation at intermediate compositions, such as x = 0.04, may arise from changes in cation arrangement and competing exchange interactions.

The remanent magnetization (M_r) varies from 29.5 to 38.00 emu g^{-1} across the series, which reflect the changes in spin arrangement and magnetic domain behaviour with Sm^{3+} substitution. The M_r/M_s ratio (R) remains consistent with ferrimagnetic ordering for all compositions. In contrast, the coercive field (H_c) increases with Sm^{3+} content. The larger coercivity may be associated with enhanced magnetocrystalline anisotropy and lattice distortion introduced by the larger Sm^{3+} ions. These structural changes can hinder domain wall movement, with the higher H_c values at x = 0.08 and 0.10 pointing to stronger domain wall pinning at defect sites and locally modified anisotropy.

The calculated magneton number (n_B), which was obtained from the molecular weight and saturation magnetization, is given in Table-4. Its variation follows the trend observed for M_s, with the highest value of 3.24 for x = 0.00 and the lowest value of 2.60 for x = 0.08. This behaviour is consistent with changes in cation distribution and A–B exchange interactions caused by Sm^{3+} substitution. The magnetic measurements therefore show that Sm^{3+} incorporation modifies both magnetization and coercivity in $CoFe_2O_4$ nanoparticles. The undoped sample retains the highest magnetic moment, while Sm^{3+} addition tends to increase the coercivity. This change in magnetic behaviour suggests that the properties of $CoFe_2O_4$ can be adjusted by controlling the Sm^{3+} content.

Photocatalytic study: Figs. 10 and 11 show the absorbance spectra of Rh-B dye in the presence of $CoFe_2O_4$ (x = 0.0) and Sm^{3+}-doped $CoFe_2O_4$ (x = 0.1) nanocatalysts, recorded at 20 min intervals. The initial spectrum exhibits the strongest absorption peak, which gradually decreases with irradiation time. After 80 min, the absorption intensity becomes very low, which indicate the substantial degradation of the dye. The degradation efficiency reaches 86.6% for pure $CoFe_2O_4$ NPs and increases slightly to 88.2% for Sm^{3+}-doped $CoFe_2O_4$ NPs. The higher efficiency of the Sm^{3+}-doped sample suggests that Sm^{3+} incorporation improves the photocatalytic response of $CoFe_2O_4$ NPs toward Rh-B degradation.

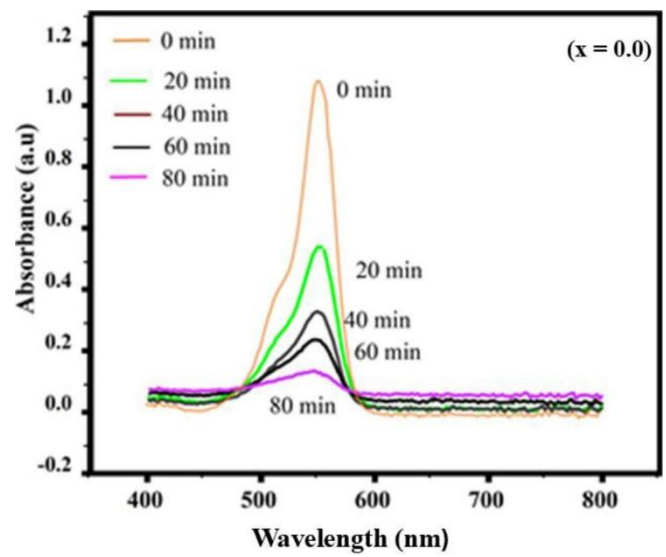

Fig. 10. Absorption spectra for rhodamine B dye degradation using $CoFe_2O_4$ NPs

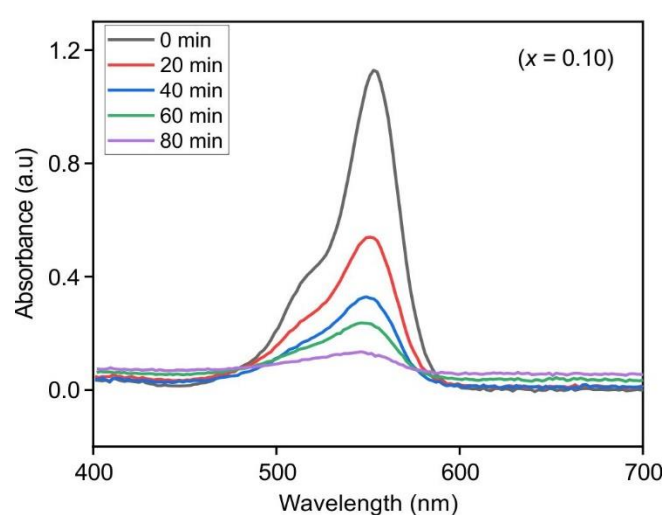

Fig. 11. Absorption spectra for rhodamine B dye degradation using $CoFe_{2-x}Sm_xO_4$ (x = 0.10) NPs

Conclusion

In this work, Sm^{3+}-doped $CoFe_2O_4$ nanoparticles with the composition $CoFe_{2-x}Sm_xO_4$ (x = 0.00-0.10) were successfully prepared and the influence of Sm^{3+} doping on their physical and magneto-optical properties was systematically established. XRD analysis proved a single-phase cubic spinel

structure with the lattice constant (a) expanding from 8.379 Å to 8.389 Å and crystallite size remaining in the 20-23 nm range, while FTIR verified the characteristic M-O vibrations of the spinel lattice. FE-SEM and HR-TEM revealed nearly spherical, partially agglomerated nanoparticles with a slight reduction in grain size upon doping and BET analysis showed a mesoporous character with surface area peaking at 15.867 $m^2 g^{-1}$ for $x = 0.04$. The optical band gap decreased from 2.69 to 2.23 eV as the Sm^{3+} content increased, which may favour visible-light-driven photocatalytic activity. All samples retained ferrimagnetic behaviour, with saturation magnetization varying from 60.17 to 77.32 emu g^{-1}. Photocatalytic tests against rhodamine B dye showed a degradation efficiency of 86.6% for pure $CoFe_2O_4$, which increased to 88.2% after Sm^{3+} doping. These results show that Sm^{3+} substitution can modify the structural, optical, magnetic and surface properties of $CoFe_2O_4$, with the resulting nanoparticles showing potential for photocatalytic applications.

ACKNOWLEDGEMENTS

The authors are grateful to Punyashlok Ahilyadevi Holkar Solapur University, Solapur, for providing the XRD measurement facility; Department of Chemistry, Dr. Babasaheb Ambedkar Marathwada University, Chhatrapati Sambhajinagar, for the FTIR facility; Institute of Chemical Technology, Marathwada Campus, Jalna, for the UV-Vis facility; and Indian Institute of Technology Madras (IIT Madras) for providing the SEM, TEM and VSM measurement facilities.

CONFLICT OF INTEREST

The authors declare that there is no conflict of interests regarding the publication of this article.

DECLARATION OF AI-ASSISTED TECHNOLOGIES

During the preparation of this manuscript, the authors used an AI-assisted tool(s) to improve the language and no data, results or scientific conclusions were generated by AI. All analyses, interpretations and conclusions are the authors' own. The authors reviewed and edited the content and take full responsibility for the published work.

REFERENCES

1. M. Mataev, A. Madiyarova, M. Abdraimova, Z. Tursyn and K. Ramachandran, *Int. J. Mol. Sci.*, **27**, 2096 (2026); https://doi.org/10.3390/ijms27052096
2. S.M. Wani, Y.P. Ubale, S.S. Gawali, J.M. Bhandari and K.M. Jadhav, *Mater. Sci. Eng. B*, **324**, 118975 (2026); https://doi.org/10.1016/j.mseb.2025.118975
3. Y. Krishnan, K. Babu, S. Sakkaraiyan, A. Dinesh, A. Shanmugam, K. Radhakrishnan and M. Ayyar, *Semiconductors*, **58**, 721 (2024); https://doi.org/10.1134/S1063782624601808
4. S.J. Salih and W.M. Mahmood, *Heliyon*, **9**, e16601 (2023); https://doi.org/10.1016/j.heliyon.2023.e16601
5. M. Umar, N. Mahmood, S.U. Awan, S. Fatima, A. Mahmood and S. Rizwan, *RSC Adv.*, **9**, 17148 (2019); https://doi.org/10.1039/C9RA03064F
6. K.A. Gurav, S. Gawali, S.M. Wani, A.P. Keche and K.M. Jadhav, *J. Supercond. Nov. Magn.*, **39**, 98 (2026); https://doi.org/10.1007/s10948-026-07198-5
7. N. Paras, K. Yadav, P. Kumar, D.R. Teja, S. Chakraborty, M. Chakraborty, S.S. Mohapatra, A. Sahoo, M.M. Chou, C.T. Liang and D.R. Hang, *Nanomaterials*, **13**, 160 (2022); https://doi.org/10.3390/nano13010160
8. S.M. Wani, P.S. Patil, S.S. Gawali, J.M. Bhandari and K.M. Jadhav, *Solid State Commun.*, **416**, 116476 (2026); https://doi.org/10.1016/j.ssc.2026.116476
9. I. Dumitru and O.F. Caltun, In *Ferrite Nanostructured Magnetic Materials*, pp. 733-745. Woodhead Publishing, 2023. https://doi.org/10.1016/B978-0-12-823717-5.00017-6
10. M. Pardavi-Horvath, *J. Magn. Magn. Mater.*, **215-216**, 171 (2000); https://doi.org/10.1016/S0304-8853(00)00106-2
11. J.M. Gonçalves, L.V. de Faria, A.B. Nascimento, R.L.G. Schermitsch, S. Patra, L.P. Hernández-Saravia, J.A. Bonacin, R.A.A. Munoz and L. Angnes, *Anal. Chim. Acta*, **1233**, 340362 (2022)' https://doi.org/10.1016/j.aca.2022.340362
12. M. Patil, K. Patel, Y. Abhale, A.P. Larios, D. Kumar, A. Chauhan, A. Marzban, M.S. Jabir and S. Ghotekar, *J. Cluster Sci.*, **36**, 71 (2025); https://doi.org/10.1007/s10876-025-02790-6
13. B.I. Kharisov, H.R. Dias and O.V. Kharissova, *Arab. J. Chem.*, **12**, 1234 (2019); https://doi.org/10.1016/j.arabjc.2014.10.049
14. R. Srivastava and B.C. Yadav, *Int. J. Green Nanotechnol.*, **4**, 141 (2012); https://doi.org/10.1080/19430892.2012.676918
15. D.O. Alshahrani, M. Arslan and M. Saad, *Ceram. Int.*, **52**, 17282 (2026); https://doi.org/10.1016/j.ceramint.2026.02.313
16. M.E. Sonawane, K.P. Gattu, V.V. Kutwade, D.A. Tonpe, F.M. Khan, S. Shaikh, P.S. Gajbar and R.B. Sharma, *Indian J. Phys. Proc. Indian Assoc. Cultiv. Sci.*, **99**, 1133 (2025); https://doi.org/10.1007/s12648-024-03327-9
17. K.M. Metha, E.R. Kumar, R. Rajamani and L.S. Wong, *Catal. Surv. Asia*, **30**, 233 (2026); https://doi.org/10.1007/s10563-026-09478-5
18. P. Thakur and A. Thakur, in eds.: A. Thakur, P. Thakur and S.P. Khurana, Nanomaterials, their types and Properties, In: Synthesis and Applications of Nanoparticles, Springer: Singapore, p. 19 (2022)
19. S. Jauhar, J. Kaur, A. Goyal and S. Singhal, *RSC Adv.*, **6**, 97694 (2016); https://doi.org/10.1039/C6RA21224G
20. M. Sangmanee and S. Maensiri, *Appl. Phys., A Mater. Sci. Process.*, **97**, 167 (2009); https://doi.org/10.1007/s00339-009-5256-5
21. S.M. Ansari, A. Younis, Y.D. Kolekar and C.V. Ramana, *Appl. Phys. Rev.*, **12**, 021308 (2025); https://doi.org/10.1063/5.0244555
22. C.S. Shinde, N.D. Sali, S.K. Dhawale, V.N. Dhanwate and V. Jawale, *Cureus J. Eng.*, **2**, es44388-024-02854-9 (2025); https://doi.org/10.7759/s44388-024-02854-9
23. R. Jasrotia, J. Prakash, Y.B. Saddeek, A.H. Alluhayb, A.M. Younis, N. Lakshmaiya, C. Prakash, K.A. Aly, M. Sillanpää, Y.A.M. Ismail, A. Kandwal and P. Sharma, *Coord. Chem. Rev.*, **522**, 216198 (2025); https://doi.org/10.1016/j.ccr.2024.216198
24. G. Katoch, Himanshi, R. Jasrotia, J. Prakash, A. Verma, A. Kandwal, S.K. Godara, R. Verma, V. Raja and G. Kumar, *Mater. Today Proc.*, (2023); https://doi.org/10.1016/j.matpr.2023.03.585
25. M. Sumalatha, P. Nagaraju and M. Sreenath Reddy, *Phys. Scr.*, **101**, 142001 (2026); https://doi.org/10.1088/1402-4896/ae58fd
26. B. Zheng, J. Fan, B. Chen, X. Qin, J. Wang, F. Wang, R. Deng and X. Liu, *Chem. Rev.*, **122**, 5519 (2022); https://doi.org/10.1021/acs.chemrev.1c00644
27. S.K. Samal, S. Kulkarni, J. Yadav and B.S. Naidu, in eds.: R.S. Ningthoujam and A.K. Tyagi, Rare-Earth Ions-Doped Nanomaterials for Photocatalytic Applications, In: Handbook of Materials Science, vol. 4: Photocatalytic Materials, Springer Nature Singapore: Singapore pp. 275-307 (2026).
28. P.N. Ukey, K.P. Patra, R.M. Meshram, D.S. Choudhary, G.K. Sukhadeve and P.B. Wasnik, *J. Mater. Sci.*, **61**, 20854 (2026); https://doi.org/10.1007/s10853-026-13058-3
29. A.S. Alsubaie, G. Raddaoui, K. Souifi, E. Berdimurodov and K. Berdimuradov, *Braz. J. Phys.*, **55**, 291 (2025); https://doi.org/10.1007/s13538-025-01915-6

30. R. Bortnic, A. Szatmari, T. Dragoiu, R.G. Hategan, R. Atanasov, L. Barbu-Tudoran, C. Tiusan, R. Lucacel-Ciceo, R. Dudric and R. Tetean, *Nanomaterials*, **15**, 1152 (2025); https://doi.org/10.3390/nano15151152
31. K. Karunasri, N.V.K. Prasad, Ramalaxmaiah, N.H. Kumar, K. ChandrababuNaidu and J. Bhemarajam, *Mater. Chem. Phys.: Sustain. Energy*, **4**, 100033 (2025); https://doi.org/10.1016/j.macse.2025.100033
32. S.S. Kadam, V.D. More, M.R. Patil, S.E. Shirsath, A.V. Fulari, V.S. Shinde, S.S. Kammar, R.H. Kadam and A.B. Kadam, *J. Magn. Magn. Mater.*, **630**, 173420 (2025); https://doi.org/10.1016/j.jmmm.2025.173420
33. D. Narsimulu, B.N. Rao, G. Nagaraju, J.S. Yu and N. Satyanarayana, *J. Solid State Electrochem.*, **24**, 225 (2020); https://doi.org/10.1007/s10008-019-04484-2
34. S.A. Bhat, A.M. Tantray, J.U. Ahsan and M. Ikram, *Ceram. Int.*, **50**, 26220 (2024); https://doi.org/10.1016/j.ceramint.2024.04.362
35. O. Oulhakem, M. Belaiche, M. El Ansary, M.A. Lemine, B. Salameh, A.K.M. Alsmadi and K.B. Alaoui, *Environ. Sci. Pollut. Res. Int.*, **31**, 57623 (2024); https://doi.org/10.1007/s11356-024-34978-0
36. K. Chandel, J. Singh, K. Kaur, C.M. Murphy, G.P. Singh and K.J. Singh, *Ceram. Int.*, **51**, 44189 (2025); https://doi.org/10.1016/j.ceramint.2025.07.150
37. R. Jasrotia, A.A. Chaudhary, S. Kumari, B. Lal, A. Sharma, Suman, H.A. Rudayni and P. Kumar, *J. Sol-Gel Sci. Technol.*, **115**, 1598 (2025); https://doi.org/10.1007/s10971-025-06868-5
38. G. Kumar, R. K. Kotnala, J. Shah, V. Kumar, A. Kumar, P. Dhiman, and M. Singh, *Phys. Chem. Chem. Phys.*, **19**, 16669 (2017); https://doi.org/10.1039/C7CP01993A
39. I. Shakir, M.N. Akhtar, S. Gulbadan and M.A. Khan, *Chem. Inorg. Mater.*, **9**, 100152 (2026); https://doi.org/10.1016/j.cinorg.2026.100152
40. V.R. Jadhav, B.R. Baburao, S.M. Rathod, S.V. Chavan, A.C. Mehere and M. Dhiware, *Solid State Sci.*, **154**, 107585 (2024); https://doi.org/10.1016/j.solidstatesciences.2024.107585
41. K. Rajashekhar, G. Vinod, K. Mahesh Kumar, G. Harikishan and J. Laxman Naik, *J. Rare Earths*, **41**, 1736 (2023); https://doi.org/10.1016/j.jre.2022.09.011
42. S. Thankachan, B.P. Jacob, S. Xavier and E.M. Mohammed, *J. Magn. Magn. Mater.*, **348**, 140 (2013); https://doi.org/10.1016/j.jmmm.2013.07.065
43. A. Jain, K. Kandwal, R. Kumar, S. Sharma, R. Dhiman, H. Sharma, K.S. Naidu, S. Gupta, A. Kumar and R. Singh, *J. Inorg. Organomet. Polym. Mater.*, **35**, 8083 (2025); https://doi.org/10.1007/s10904-025-03676-w
44. S.P. Nawale, P.B. Dube, S.M. Wani, A.P. Keche and K.M. Jadhav, *Solid State Commun.*, **416**, 116489 (2026); https://doi.org/10.1016/j.ssc.2026.116489
45. V.R. Bhagwat, A.V. Humbe, S.D. More and K.M. Jadhav, *Mater. Sci. Eng. B*, **248**, 114388 (2019); https://doi.org/10.1016/j.mseb.2019.114388
46. A. Sutka and G. Mezinskis, *Front. Mater. Sci.*, **6**, 128 (2012); https://doi.org/10.1007/s11706-012-0167-3
47. C. Longchar, A.R. Xavier and D. Nath, *Res. Dig. Eng. Manage. Soc. Innov.*, **1**, 29 (2025); https://doi.org/10.46647/ayy33561
48. M.T. Kotkar, S.M. Wani, P.G. Shinde, A.G. Patil and K.M. Jadhav, *Solid State Commun.*, **400**, 115914 (2025); https://doi.org/10.1016/j.ssc.2025.115914
49. S. Gawali, S.M. Wani, Y.P. Ubale, P.S. Patil, K. Deshmukh and K.M. Jadhav, *Mater. Sci. Eng. B*, **323**, 118846 (2026); https://doi.org/10.1016/j.mseb.2025.118846
50. N.P. Prasetya, R.I. Setiyani, Utari, K. Kusumandari, Y. Iriani, J. Safani, A. Taufiq, N.A. Wibowo, S. Suharno and B. Purnama, *Mater. Res. Express*, **10**, 036102 (2023); https://doi.org/10.1088/2053-1591/acc011
51. K.K. Deshmukh, P.S. Patil, S.D. Tapsale, A.P. Keche and K.M. Jadhav, *Mater. Sci. Eng. B*, **323**, 118807 (2026); https://doi.org/10.1016/j.mseb.2025.118807
52. C.V. Ramana, Y.D. Kolekar, K. Kamala Bharathi, B. Sinha and K. Ghosh, *J. Appl. Phys.*, **114**, 183907 (2013); https://doi.org/10.1063/1.4827416
53. Q.Y. Tamboli, P.D. Mhase, I. Bushnak, A.M. Alshehri, A.G. Al-Sehemi, S.M. Patange and K.R. Zakde, *Solid State Sci.*, **168**, 108041 (2025); https://doi.org/10.1016/j.solidstatesciences.2025.108041
54. S.M. Wani, M.T. Kotkar, R.G. Vidhate, J.M. Bhandari and K.M. Jadhav, *Phys. Scr.*, (2024); https://doi.org/10.1088/1402-4896/ada3fd
55. L.S. Kumar, *R. Soc. Open Sci.*, **13**, 251523 (2026); https://doi.org/10.1098/rsos.251523
56. S.S. Rani, A. Purnakanti, P. Naveen, P. Sowjanya, P.G. Pavani, M.C. Rao, N. Kumar Swamy and N.P. Kumar, *Next Mater.*, **13**, 102613 (2026); https://doi.org/10.1016/j.nxmate.2026.102613
57. M.M. Khan, S.A. Ansari, D. Pradhan, M.O. Ansari, D.H. Han, J. Lee and M.H. Cho, *J. Mater. Chem. A Mater. Energy Sustain.*, **2**, 637 (2014); https://doi.org/10.1039/C3TA14052K